Three dimensional quantification of soil hydraulic properties using X-ray Computed Tomography and image based modelling

Author list: Saoirse R. Tracy[1$], Keith R. Daly[2$], Craig J. Sturrock[1], Neil M. J. Crout[1], Sacha J. Mooney[1], Tiina Roose[2§]

Author affiliations:

[1] School of Biosciences, University of Nottingham, Sutton Bonington Campus, Leicestershire, LE12 5RD.

[2] Bioengineering Sciences Research Group, Faculty of Engineering and Environment, University of Southampton, University Road, SO17 1BJ.

[$] These authors are joint lead authors

[§] Corresponding author: Bioengineering Sciences Research Group, Faculty of Engineering and Environment, University of Southampton, University Road, SO17 1BJ Southampton, United Kingdom, email: t.roose@soton.ac.uk

Key Points:

- X-ray Computed Tomography is used to image water distribution in soil.
- 3D Computed Tomography images are combined with image based modelling.
- Unsaturated hydraulic conductivity and the water release characteristic are obtained.

1. Abstract

We demonstrate the application of a high-resolution X-ray Computed Tomography (CT) method to quantify water distribution in soil pores under successive reductive drying. We focus on the wet end of the water release characteristic (WRC) (0 to -75 kPa) to investigate changes in soil water distribution in contrasting soil textures (sand and clay) and structures (sieved and field structured), to determine the impact of soil structure on hydraulic behaviour. The 3D structure of each soil was obtained from the CT images (at a 10 μm resolution). Stokes equations for flow were solved computationally for each measured structure to estimate hydraulic conductivity. The simulated values obtained compared extremely well with the measured saturated hydraulic conductivity values. By considering different sample sizes we were able to identify that the smallest possible representative sample size which is required to determine a globally valid hydraulic conductivity.

Keywords: Matric potential; soil pores; water release characteristic; X-ray Computed Tomography; image based homogenisation.

Abbreviations:

(3D) - 3-dimensional

(CT) - Computed Tomography

(ROI) - Region of interest

(WRC) – Water release characteristic

(WFP) – Water filled pores

(AFP) – Air filled pores

(REV) -Representative elementary volume

Short title for page headings: Three-dimensional quantification of soil hydraulic properties

Deleted:

2. Introduction

Understanding the dynamic nature of water movement through, and storage within, soil is of fundamental importance for most of its functions. A more detailed knowledge of how soil structure influences soil water distribution and subsequently availability to plants is needed to inform soil management practices and thus contribute to efforts in increasing crop yields for an expanding global population. However, to truly understand how water moves through soil and is retained in soil pores whilst undergoing drying, non-destructive measurements of the soil aggregate geometries and pore structure are needed. The use of X-ray Computed Tomography (CT) to examine the 3D soil pore structure is rapidly gaining pace [*Helliwell et al.*, 2014; *Mooney et al.*, 2012]. The ability to segment water from a greyscale CT image remains challenging due to limitations in the phase separation achievable with regular detectors in benchtop CT scanners. Segmentation of fluids in alternative porous media such as glass beads has been previously described in the literature [*Haugen et al.*, 2014; *Iassonov et al.*, 2009]. However, due to the more complex, heterogeneous structure of soil and the associated challenges faced during image acquisition this brings, these segmentation techniques cannot always be readily applied to the segmentation of soil phases in X-ray CT images [*Houston et al.*, 2013]. Yet, Crestana *et al.* [1985] highlighted the potential of CT for investigating water movement through soil by quantifying the vertical and lateral water flows in 3D. By using dual

Deleted: well documented

Deleted: be easily

Deleted: using

energy tomography Rogasik *et al.* [1999] showed it is possible to quantify soil water, pore space and bulk density. Mooney [2002], compared dry and moist samples and developed an imaging method to separate water from the bulk soil in undisturbed soil cores albeit at a coarse resolution (0.5 mm) using a medical CT scanner. Water flow characteristics were well matched to macropore structure, with *circa* 90% of macropore space active in water transport in a sandy clay texture, compared to *circa* 50% in the sandy loam soil. Wildenschild *et al.* [2005] investigated multiphase flow processes and quantified drainage paths showing that water is preferentially lost from larger pores and the drainage of the remaining disconnected pores is prevented. Since then Tippkotter *et al.* [2009] detected soil water in macropores and measured water film thickness at a 20 μm resolution. They quantified the water without the use of contrast enhancing agents or comparison of wet and dry scans. Partial volume effects make separating boundaries between phases of interest a challenging task, due to the material of concern often failing to fully fill a voxel [*Ketcham and Carlson*, 2001]. This can lead to individual voxels being misclassified. However, as a microfocus system with a fine resolution was used in the study, the impact of voxel misclassification is minimised [*Clausnitzer and Hopmans*, 2000]. The most recent advances in CT imaging technology now allow 3D non-destructive imaging of soils at even higher resolutions, *e.g.* <3 μm spot size [*Zappala et al.*, 2013], allowing water to be observed in smaller pores than previously considered.

The macroscopic scale flow in saturated and unsaturated porous media are often described using a Darcy's law and Richards' equation [*Hornung*, 1997]. These equations are parameterised by the unsaturated hydraulic conductivity and WRC. From a mathematical perspective Darcy's law can be derived from the underlying Stokes equations using the method of homogenization [*Keller*, 1980]. This approach has been applied to single porosity materials [*Hornung*, 1997; *Keller*, 1980], double porosity materials [*Arbogast and Lehr*, 2006; *Panfilov*,

Deleted: c.*circa* 0.5 mm
Formatted: Font: Not Italic
Deleted: similar to
Deleted: *c.*
Deleted: *c.*
Deleted: , they
Deleted: ed
Deleted:

2000], and porous media containing voids or vugs [*Arbogast and Lehr*, 2006; *Daly and Roose*, 2014]. This method is based on the idea that the underlying porous structure is periodic, *i.e.*, it is composed of a set of regular repeating units. By calculating the average fluid velocity for a single representative unit volume due to a unit pressure drop, Darcy's law and the representative hydraulic conductivity can be derived [*Pavliotis and Stuart*, 2008; *Taylor et al.*, 1970]. The mathematics underlying the WRC is less well established and homogenization studies to date have assumed that the air water interface is known in advance [*Taylor et al.*, 1970].

Image based modelling can be loosely divided into two categories: pore network modelling and direct simulation [*Blunt*, 2001; *Blunt et al.*, 2013]. The first of these, pore network modelling, refers to the extraction of a representative network from the pore scale geometry [*Fatt*, 1956] and has been widely used to predict averaged properties of packed spheres [*Bryant and Blunt*, 1992; *Bryant et al.*, 1993b] and imaged porous media [*Blunt, 2001; Blunt et al.*, 2013; *Bryant et al.*, 1993a]. This technique is able to reproduce relative permeability curves and water release characteristics. However, the pore network extraction results in a simplified geometry which may neglect important pore scale phenomena. The alternative technique of direct modelling involves solving equations directly on the imaged geometries. This technique captures the detail of the pore scale geometry down to the resolution limit. The key disadvantage is that modelling multiphase flow is demanding from a computational point of view. Typically models of this type are based on Lattice Boltzman simulations of two fluids as these are highly parallel and relatively easy to implement [*Gao et al.*, 2012; *Ramstad et al.*, 2010]. Other image based modelling studies in porous media include 3D image based simulations of nutrient transport [*Keyes et al.*, 2013] and saturation based flow modelling of water movement in 2-D image slices [*Aravena et al.,* 2014; *Aravena et al.,* 2011].

In this paper we demonstrate the application of a high resolution CT method to quantify water distribution in soil pores under successive reductive drying. Using the structural geometries from the CT images we apply the method of homogenization combined with direct image based modelling to calculate the hydraulic conductivity across a range of matric potentials. This can be seen as analogous to the measurement of a wetting phase relative permeability curve. Specifically the question we aimed to answer is: what is the smallest possible Representative Elementary Volume (REV) required to determine a hydraulic conductivity approximation which is globally valid? In addition the soil moisture content is calculated directly from the CT images at a range of different matric potentials and, hence, the WRC is derived. This approach is chosen, rather than Lattice Boltzmann simulation, as it allows the WRC and hydraulic conductivity to be calculated quickly without the need for time consuming two fluid simulations. From the images we are able to obtain information on soil drainage in both undisturbed field cores and sieved soils. This was used to accurately determine the impact of soil structure on hydraulic behaviour.

3. Materials and Methods

Deleted: ¶

3.1. Sample preparation

Soil was obtained from The University of Nottingham farm at Bunny, Nottinghamshire, UK (52.52° N, 1.07° W). The soils used in this study were a Eutric Cambisol (Newport series, loamy sand/sandy loam) and an Argillic Pelosol (Worcester series, clay loam). Particle size analysis for the two soils was: 83% sand, 13% clay, 4% silt for the Newport series and 36% sand, 33% clay, 31% silt for the Worcester series. Typical organic matter contents were 2.3%

for the Newport series and 5.5% for the Worcester series [*Mooney and Morris, 2008*]. From herein the two soil types are referred to as sand and clay soil. Loose soil was collected from each site in sample bags and field cores (10 mm height, 10 mm diameter) were collected from the immediate soil surfaces after any residues had been cleared. Four replicates were collected for each soil type. Saturated hydraulic conductivity measurements of the field cores were obtained via the standard laboratory method using a constant head device [*Rowell*, 1994]. Experimentally obtained hydraulic conductivity measurements were made for comparison with the calculated values.

3.2. Measurement of the soil water release characteristic

In order to investigate the effect of drying on soil water distribution and soil structural changes in 3D, a custom-built tension table was designed to hold the soil sample at a given matric potential, whilst undergoing CT scanning. A small vacuum chamber was constructed (Supplementary Figure 1), that contained a porous ceramic plate (Soil Moisture Corp, Santa Barbara, CA, U.S.A) on top of which a field soil core was placed, with kaolin clay at the base to ensure a good contact. The sample size was kept small to ensure high resolution scanning based on the sample size:resolution trade off that limits CT studies [*Wildenschild et al.*, 2002]. The porous ceramic was first submerged in de-aired deionized water and a vacuum applied to ensure no air bubbles remain trapped within the ceramic. The plastic chamber had an O-ring seal at the base and a flange, which was screwed together to ensure an air-tight fit. All components of the chamber were made from plastic to avoid possible image artefacts, which could result from using high X-ray attenuating construction materials such as metal. A 0387 Millipore vacuum pump (Merck Millipore, MA, USA) was attached to the chamber and the soil columns were initially saturated from below with deionized water before being placed

Deleted:

Deleted: put

under a vacuum of -5 kPa (50.8 mmHg), -10 kPa (76.2 mmHg), -20 kPa (152.4 mmHg), -40 kPa (304.8 mmHg), -60 kPa (457.2 mmHg) and -75 kPa (533.4 mmHg). It was not possible to achieve pressures in excess of -75 kPa in the system described. The vacuum pump was enabled for 120 min then the valve sealed to retain the vacuum inside the chamber. At each matric potential the soil core inside the chamber was scanned (further details in next section). After each scan the soil core was removed from the chamber and weighed to calculate gravimetric water content.

Deleted: Despite testing

Deleted: , further

Deleted: were not possible

Deleted: turned on

Using a combination of sand tables, pressure plates and pressure membrane apparatus, the WRC were obtained for both soil types. Using conventional methods the van Genuchten model [*van Genuchten*, 1980] was fitted to the data. The sand table was prepared by filling the water reservoir and raising it above the base height of the table to ensure full saturation of the sand table with no air bubbles. Both undisturbed field cores and sieved samples (packed to a bulk density of 1.2 g cm^{-3}) were placed flat on the sand table. To obtain the mid-range points on the WRC, a pressure plate Model 1600 Pressure Plate Extractor (Soil Moisture Corp, Santa Barbara, CA, U.S.A) was used. Samples were placed on the plate and the samples were weighed frequently until equilibrating at a series of matric potentials. To obtain measurements at lower matric potentials, a pressure membrane apparatus was used. For the sieved samples the required mass of soil was carefully placed into the metal vessels of the pressure membrane apparatus and saturated with air-free water. The field core samples were directly collected in the metal cores and placed onto the apparatus. The collection tubes were weighed frequently and once equilibrated the system was adjusted to higher pressures. After the final measurement, soil samples were oven dried at 105 $^{\circ}$C for 24 hr then weighed.

The measured volumetric water content of the field structured soil cores (θ), accounted for the likely presence of stones and their overall influence on the WRC [*Gardner*, 1965; *Reinhart*, 1961]. The volumetric water content of the soil is written as θ which is measured in $\frac{\mathrm{cm^3(H_2O)}}{\mathrm{cm^3(Soil)}}$. To calculate this a correction was applied to the measured volumetric water content of the sample, θ_m, which is measured as $\frac{\mathrm{cm^3(H_2O)}}{\mathrm{cm^3(Total)}}$. This stone correction was calculated using

$$\theta = \theta_m \left(1 + \frac{V_s}{V_f}\right), \qquad (1)$$

where V_f is the fine soil volume measured in $\mathrm{cm^3(soil)}$ and V_s is the volume of stones which is measured in $\mathrm{cm^3(stones)}$ and calculated by subtracting the soil volume from the total sample volume.

3.3. X-ray Computed Tomography and analysis

Four replicates from each soil type of the field cores were scanned at the seven matric potentials giving a total of 56 scans for the field structured cores. As they would not be used for individual pore characterisation analysis only three replicates were scanned for the sieved soils leading to 42 additional scans and a total overall number of 98 scans. The field of view for each scan included the entire sample and each scanned sample created a dataset approximately 25 gigabytes in size, which includes all the associated image stacks for analysis, therefore 2.4 terabytes of data was collected. X-ray CT scanning was performed using a Phoenix Nanotom 180NF (GE Sensing & Inspection Technologies GmbH, Wunstorf, Germany). The scanner consisted of a 180 kV nanofocus X-ray tube fitted with a diamond transmission target and a 5-megapixel (2316 x 2316 pixels, 50 x 50 μm pixel size) flat panel detector (Hamamatsu Photonics KK, Shizuoka, Japan). A maximum X-ray energy of 100 kV and 140 μA was used

Deleted: giving a total of

Deleted: so overall

to scan each soil core. A total of 1440 projection images were acquired over a 360° rotation. Each projection was the average of 3 images acquired with a detector exposure time of 1 s. The resulting isotropic voxel edge length was 10.17 μm and total scan time was 105 minutes per core. Although much faster scan times are possible it was necessary in this instance to use a longer scan time to acquire the highest quality images to aid with the phase separation. Two small aluminium and copper reference objects (< 1 mm^2) were attached to the side of the soil core to assist with image calibration and alignment during image analysis. Reconstruction of the projection images to produce 3D volumetric data sets was performed using the software datos|rec (GE Sensing & Inspection Technologies GmbH, Wunstorf, Germany).

The reconstructed CT volumes were visualised and quantified using VG StudioMAX® 2.2 (Volume Graphics GmbH, Heidelberg, Germany). Air, soil and water phases of the scanned volume were segmented separately using a threshold technique based on the greyscale value of each voxel using a calibration tool within VG StudioMax v2.2. This works by selecting specific areas of the scanned volume based on greyscale values, which are a result of (X-ray attenuation) density differences within the sample. Image segmentation is the classification of voxels within a CT volume that share common grayscale values and thus X-ray attenuation. The calibration tool allows the user to sample the greyscale value of a selection of voxels that correspond to the background (*e.g.* the phase/s not considered, this is usually the background air) and then the process is repeated for voxels that correspond to the material of interest (*e.g.* water, air or soil). Based on the greyscale range we segmented all voxels above a 50% mean value between the background and material of interest and define them as a particular phase (i.e. a region of interest). In a two phase sample air is usually used as the background greyscale value to calibrate against. However, as we required the segmentation of three phases, two

Deleted: inside each chamber for each scan vessels, one containing soil pore water and the other finely sieved soil (< 100 μm) for either the sand or clay soil were securely fitted to the inside of the chamber for each scan. The soil pore water and finely sieved soil remained separate from the soil core, but within the imaging field of view, which was important as the soil core sample can change in overall greyscale range over the course of the experiment due to localised drying and X-ray filament aging. Using this approach these separate vessels were used as reference objects during image analysis. It was important that reference vessels were included in every scan as CT scanning is subject to minor variations in greyscales between scans as the system filament ages. A schematic representation of the water segmentation method is presented in Supplementary Figure 2. The first stage was to create a region of interest (ROI) that included all phases except the air filled pore space. This was done by selecting the air space around the sample as the background, ensuring all voxels except those of air would be included as the material of interest and a 3D ROI was then created and labelled 'Water and soil ROI' *e.g.* air not included. The process was then repeated, but utilising the soil inside the reference vessel as a reference value for the solid material. It was used as a reference as it contained limited water and air, hence this 3D ROI was labelled 'Soil'. Subtraction of the 'Soil ROI' from the 'Water and soil ROI' resulted in a ROI with voxels of grey scale values attributed to 'soil water only', *e.g.* the range of voxels remaining after the soil and air ROIs have been subtracted. The volume of the resulting 'Soil Water' ROI was validated against the water reference object and traditional methods of determining volumetric water content (weighing). Using this approach we assume all organic matter is classified as 'soil'. To create an ROI that included solely the air filled pore space, the ROI that included all material except the air was inverted using the 'Invert ROI' function in VG StudioMax software. The volume analyser tool in VG StudioMax was subsequently used to quantify the total volume of the air and water filled pores. Reconstructed volumes for each matric potential were aligned in VG StudioMax using the metal reference objects on the outside

Deleted: throughout
Deleted: i
Deleted: a
Deleted: everything, but
Deleted: everything else
Deleted: was
Deleted: used
Deleted: that
Deleted: just
Deleted: everything but
Deleted:
Deleted: manually
Deleted:

of the sample container. After segmentation of the soil core volumes, a cylindrical ROI shape template was used to subtract the surrounding column and air space from the volume to remove the cylinder of soil. This template was used to ensure the same volume was used for each sample before analysis. No significant evidence of shrinkage was observed across the range of low matric potentials considered here. We note that when three phases (air water and soil) are present in an image erroneous films of the intermediate phase can often be segmented out between the high and low density phases. In this case erroneous films of water could be introduced through segmentation. However, as thin water films only contribute a total flow proportional to the third power of the film thickness these are not a concern in this study.

Image stacks of the extracted volumes were exported and subsequently analysed for individual water filled and air filled pore characteristics for the field structured soil only using ImageJ v1.42 (http://rsbweb.nih.gov/ij/) [*Ferreira and Rasband*, 2011]. For 2D analysis objects less than two pixels (twice the resolution) in diameter (0.02 mm) and for 3D analysis objects less than two voxels in each direction (8×10^{-6} mm^3) were regarded as potential noise as a precaution [*Wildenschild et al.*, 2005] and subsequently excluded from the analysis. The BoneJ plugin algorithm [*Doube et al.*, 2010] (http://bonej.org/) in ImageJ software was used to measure discrete individual 3D water filled and air filled pore characteristics namely volume, surface area and thickness (diameter). A voxel is classed as connected to another voxel if it at least touches corner to corner. ImageJ was used to measure the 2D pore shape characteristic 'circularity', which is a measure of an object's similarity to a circle. A value of 1 describes a perfect circle and as the value decreases, the object becomes increasingly elongated. The circularity was determined using

$$C = \frac{4\pi(A_p)}{(P_p)^2}, \qquad (2)$$

Deleted: cropped

Deleted: 20 µm

Deleted: 80 µm³

Deleted: and subsequently excluded from the analysis

Deleted: .

Deleted: -

Deleted: perfect

Deleted: would be

where A_p is the pore area and P_p is the pore perimeter. The water-filled pore image stack was skeletonised and from this the 3D connectivity (the sum of all the thin (1 voxel) pathways that still preserve the connected topology and original shape of the object) of the water-filled pore volume was also calculated.

In order for the geometries of the water-filled pores to be modelled, surface mesh files (.stl) were required which were generated in VG StudioMax v2.2. After segmentation of the soil water phase, a cube shaped ROI template was imported to create identical cubes for the surface mesh generation. Each sample was subsampled, from random initial coordinates, with 6 cubes comprising side lengths of 3.8 mm. The same coordinates were used for different matric potentials of the same sample. Each individual surface mesh file took between 0.5 – 2 hours to generate depending on the complexity of the surface.

3.4. *Modelling*

The hydraulic conductivity of the soil was calculated using the method of homogenization [*Pavliotis and Stuart*, 2008]. This method allows an average Darcy's law to be defined which is applicable to the soil column and is parameterised by the pore scale geometry of the soil. The key assumption used was that the hydraulic properties of the soil can be accurately captured by studying a small subsample of the soil [*Fowler*, 1997], this is often referred to as the Representative Elementary Volume (REV). In this paper we were particularly interested in determining the minimum size REV for which the calculated hydraulic conductivity converges to the macroscopic hydraulic conductivity for soil samples of the order of a few millimetres.

Moved (insertion) [1]

Deleted: ; these

Moved up [1]: In order for the geometries of the water-filled pores to be modelled, surface mesh files (.stl) were required; these were generated in VG StudioMax v2.2. After segmentation of the soil water phase, a cube shaped ROI template was imported to create identical cubes for the surface mesh generation. Each sample was subsampled, from random initial coordinates, with 6 cubes comprising side lengths of 3.8 mm. The same coordinates were used for different matric potentials of the same sample. Each individual surface mesh file took between 0.5 – 2 hours to generate depending on the complexity of the surface.

Deleted: ¶

This method allowed us to theoretically determine the required sample size for CT analysis of water flow in soil at this scale.

Deleted: on

Deleted: ¶

We note that the averaged hydraulic conductivity and WRC calculated at this scale are not globally applicable. Rather they describe the average flow rate in soil of this type assuming no large scale features such as cracks or larger voids are encountered. In theory these features could be included by deriving an averaged Darcy's law for each soil type, Stokes' equations for large void spaces and approximate Darcy's laws for fractures equation [*Hornung*, 1997]. These systems could, in principle, be upscaled to derive averaged Darcy's laws on a much larger scale. However, in this paper our focus is in obtaining an estimate of the hydraulic properties of soils based on their pore structure. Hence, we neglect these larger scale features but emphasise that they could be included through an additional level of upscaling.

Deleted: on

Deleted: that

Deleted: ,

Deleted: or regions of different porosity

Deleted: we are interested

As we are able to segment the air and water separately from the CT images, the fluid dynamics can be greatly simplified. Rather than focusing on the moving interface between each phase, we consider the relatively slow, flow of water about a fixed interface. The resulting equations are introduced in the appendix. We further simplify the equations by assuming that the non-wetting phase, in this case air, is stationary. This assumption is valid assuming that the air phase is disconnected. If this is not the case then the movement of the air effectively lubricates the movement of water resulting in an increase in the hydraulic conductivity. This approach is valid assuming that the pressure gradients are sufficiently low, such that the interface remains fixed, and that the non-wetting phase is not connected, hence, the trapped non-wetting phase has zero average velocity.

Deleted: consider

Strictly speaking the theory of homogenization requires the soil structure to be periodic. Clearly for real soil samples this is not the case. This is overcome by enforcing an apparent image based periodicity either by translation or reflection of the CT image (Figure 1). In this paper reflection was chosen as it simplifies the resulting calculations and does not introduce discontinuities in the soil structure. The error induced by enforcing periodicity is that the geometry considered numerically is now fully periodic rather than quazi-periodic and does not truly represent the imaged soil structure. To overcome this, different size REVs were taken from the segmented .stl files, see Figure 1. Specifically, the 6 cubes which were segmented from each scan were of the same volume $V_m = 54.9\ \mathrm{mm}^3$, and were assumed to be sufficiently large that the soil properties would have converged. The REVs sampled from the six cubes were of volume $V = V_m/(2^j)$, where j is a positive integer in the range 0 to 10 such that the smallest volume we consider is 0.053 mm^3 and the largest is V_m. As j is decreased and, hence, the size of the REV is increased, the relative size of the errors induced by the reflection decreases. Similarly as the REV size increases, the hydraulic properties of the subsample will, in principle, converge to the hydraulic properties of the soil.

Deleted: n

Deleted: n

Deleted: 8

Deleted: 2

Deleted: n

A rigorous analysis of equations governing fluid flow through soil is given in [*Daly and Roose*, 2014]. Here we provide a brief description of the theory in the applied context with further details given in the appendix. We consider a sample of soil which is large with respect to the REV size. Specifically if the REV is a small cube with side length L_y and the large sample we are interested in has characteristic length L_x then we require that the ratio of these two lengths is small, *i.e.*, $\epsilon = L_y/L_x \ll 1$. For typical pore sizes observed in soil, the viscous forces dominate [*Fowler*, 1997]. Hence, we may consider the Stokes limit of the Navier-Stokes equations where all inertial terms are neglected. Mathematically the macroscopic hydraulic conductivity, which is valid for the whole soil column, is obtained in two steps. First, it is shown, see appendix for details, that pressure variations across the REV of size ϵ will induce a water velocity also of size ϵ. Secondly, a set of equations are derived which allow the pressure driven fluid velocity to be determined based on the soil (Figure 1). Finally, the average velocity over the REV is used to determine a Darcy's law which is independent of ϵ. This value is valid for the bulk soil and describes fluid driven by an external pressure gradient, see [*Daly and Roose*, 2014]

Deleted: '

Deleted: unit cell

Deleted: only affect the average water

Deleted: by a quantity

$$\boldsymbol{u} = -\mathcal{K}(\boldsymbol{\nabla} p_0 - \rho g \hat{\boldsymbol{e}}_z), \tag{3}$$

where ρ is the fluid density ($\rho = 10^3 \text{kg m}^{-3}$ in the case of water), $g = 9.8 \text{ m s}^{-2}$ is the acceleration due to gravity, p_0 is the applied pressure, $\boldsymbol{u}$ is the volume averaged water velocity and $\mathcal{K}$ is the relative permeability (in the general case a tensor) which has components defined as

$$\mathcal{K}_{jk} = \frac{L_y^2}{\mu} \int_{\Omega_w} \hat{\boldsymbol{e}}_j \cdot \boldsymbol{v}_k^w \, dy. \tag{4}$$

Here $\hat{\boldsymbol{e}}_j$, for $j = x, y, z$ is a unit vector in the j-th direction and $\boldsymbol{v}_k^w$ is the local velocity. Assuming that the air velocity is slower than the water velocity then $\boldsymbol{v}_k^w$ satisfies the cell problem

$$\boldsymbol{\nabla} \cdot \sigma_k^w - \boldsymbol{\nabla} \pi_k^w = \hat{\boldsymbol{e}}_k, \qquad \boldsymbol{x} \in \Omega_w, \tag{5a}$$

$$\boldsymbol{\nabla} \cdot \boldsymbol{v}_k^w = 0, \qquad \boldsymbol{x} \in \Omega_w, \tag{5b}$$

$$\boldsymbol{v}_k^w = 0, \qquad \boldsymbol{x} \in \Gamma_s, \tag{5c}$$

$$\boldsymbol{v}_k^w = 0, \qquad \boldsymbol{x} \in \Gamma_{aw}, \tag{5d}$$

where $\sigma_k^w = (\boldsymbol{\nabla} \boldsymbol{v}_k^w) + (\boldsymbol{\nabla} \boldsymbol{v}_k^w)^T$, π_k^w is the local pressure correction due to the microscale geometry, the superscript w denotes the water phase, Ω_w, Γ_s and Γ_{aw} denote the water domain, the soil boundary and the air-water interface respectively. Physically this can be thought of as calculating the fluid velocity subject to a unit pressure gradient. As the equations are linear Darcy's law follows by multiplying the result by the desired pressure gradient.

Equations (5) were solved numerically on each subsample obtained from the CT images using OpenFOAM, an open source Computational Fluid Dynamics toolbox running on IRIDIS, the High Performance Computing Facility at the University of Southampton. The hydraulic conductivity is then calculated as the average water velocity due to gravity. Results were obtained for each soil sample using the method illustrated in Figure 1. The 6 cube surface meshes, generated from each soil core, were repeatedly sampled to obtain 3D REVs of increasing size. The result is a set of hydraulic conductivity calculations which we expect to converge to the true hydraulic conductivity of the soil, at each point along the WRC, as the sub-volume size is increased.

3.5. Statistical analysis

The results obtained directly from the CT images were analysed by general analysis of variance (ANOVA) containing soil type and matric potential and all possible interactions as explanatory variables using Genstat 15.1 (VSN International, UK).

4. Results & Discussion

4.1 Hydraulic properties

The clay soil contained an average stone volume of 0.2 cm^3 whereas the average stone volume for the sand soil was 5.5 cm^3 (total soil volume was 55 cm^3). Therefore although field structured soil was able to retain water for longer, as shown by the curves from the conventional method (Figure 2), the influence of stones was not a consideration and the greater water holding capacity is attributed to the more complex pore network in the field structured soil.

There are clear differences between sieved soil and field structured soil (Figures 2 and 3). For the field structured soil the imaging technique shows a good agreement with the conventional methods with an average error of ≤ 5% across the range of matric potentials considered. The sieved soil responded more strongly to pressure change in comparison to the field structured soil. However, the imaged sieved soil data did not show this trend, hence, there was quite a large error of 9% at 0 kPa and as high as 65% at -75 kPa. This suggests that, for the field structured samples, the segmentation procedure was successful at identifying the majority of the water filled pores (WFPs).

It is somewhat surprising that the more homogeneous sieved soil is less well represented through the imaging technique than the field structured soil. However, we attribute this to the pore size distribution in the two soils. The field structured soil has a wider range of pore sizes than the sieved soil which contains macropores defined by the largest grain size. As the matric potential becomes increasingly negative, the water drains from smaller and smaller pores. In

Deleted: samples

Deleted: samples

Deleted: is

Deleted: less than

Deleted: this can be

Deleted: d

Deleted: is likely

Deleted: have

Deleted: will

Deleted: is made

the case of the field structured soil this results in a gradual decrease in volumetric water content with matric potential which the imaging technique can follow assuming the pore size is larger than the image resolution. In the case of the sieved soil there is a reduced range of pore sizes and the water quickly drains from the larger pores and remains trapped in a large number of smaller pores. The result is that the volumetric water content drops quickly as the matric potential is reduced and the imaging technique, which cannot resolve the smallest pores, fails to capture this. We also note that the differences observed in the WRC between the two soil types is smaller when measured using the imaging technique than using conventional methods. This is again attributed to the finite resolution of the measurements and is analogous to the increasing error observed as the saturation is decreased.

The hydraulic conductivity, which corresponds to the water release curves shown in Figure 2, has been calculated by solving equations (5) for increasing subsample size. As the subsample size was increased, the hydraulic conductivity converged to a fixed value which we interpret as the macroscopic hydraulic conductivity (Figure 4). The sample size at which this occurred was smaller for lower matric potentials. This is attributed to the increased air-filled porosity which decreases the contact area between the water and the soil. Hence, the effect of the heterogeneous soil boundary is decreased and the overall homogeneity of the sample is increased. We note that, as convergence is seen to occur at smaller sample sizes for lower saturation, fewer simulations were run at these saturation values. This occurs at approximately ¼ of the sample volume for all matric potentials for both soils. We note that although the REV volume is approximately the same for all soil types considered, the properties obtained from this analysis are different for different soil types. This method therefore enabled the required

Deleted: the macroscopic

Deleted: values

sample size for CT analysis of water flow in these samples to be determined, which was a cube volume of 11 mm^3. This sample was large enough for convergence of the calculated hydraulic conductivity, meaning that the sample size contained an adequate volume of soil to capture the averaged hydraulic properties on this scale. Therefore considering the averaging method used in this paper, the hydraulic conductivity is globally valid. This means that the representative volume of 11 mm^3 is an appropriate representative volume element for the global hydraulic conductivity of the soil samples used in this study. However, there may be significant features, such as cracks or heterogeneities in the soil, which are not captured in the 11 mm^3 volume. Hence, care must be taken in applying these results on the field scale and an additional level of upscaling may be required to capture the properties of these features.

Deleted: soil

Deleted: We note that, due

Deleted: to

Deleted: se

Deleted: s

Deleted: some

Deleted: .

The method described in Section 3.4 and the appendix allowed us to also obtain the hydraulic conductivity in unsaturated soils as well as in *x*, *y* and *z* directions. It was expected the flow would be dominant in the *z* direction due to gravity, however (possibly due to the size of the samples) we did not observe this. The calculated hydraulic conductivities are shown as a function of matric potential in Figure 5. The calculated hydraulic conductivities and the corresponding WRC have been fitted to the van Genuchten model for the WRC and the unsaturated hydraulic conductivity [*van Genuchten*, 1980] using a non-linear least squares method. We note that we have only done this fitting for the imaged data as we do not have hydraulic conductivity measurements for the full range of matrix potentials using conventional measurements. The volumetric water content θ is given by

Deleted: that

$$\theta = (\theta_s - \theta_r)\left(\frac{1}{1+(\alpha h)^n}\right)^m + \theta_r, \tag{6}$$

where θ_s and θ_r are the saturated and residual volumetric water content respectively, h is the is the matric head, $m = 1 - 1/n$ and n and α are the van Genuchten parameters. The corresponding hydraulic conductivity is given by $K = K_{sat} k_r^{vg}$. Here K_{sat} is the saturated hydraulic conductivity and the relative hydraulic conductivity is given by

$$k_r^{vg} = \frac{\{1 - (\alpha h)^{n-1}[1 + (\alpha h)^n]^{-m}\}^2}{[1 + (\alpha h)^n]^{m/2}}. \qquad (7)$$

We take θ_r to be negligible and fit the remaining parameters to the imaged data. The average saturated hydraulic conductivity and the fitted parameters: K_{sat}, θ_s, α and n are shown in Table 1. The fitted hydraulic conductivity and WRC, obtained using these parameters, are shown in Figure 5.

[Deleted: hydraulic]

[Deleted: t]

Table 1. Fitted van Genuchten parameters

Soil	**Measured K_{sat} $[cm\ s^{-1}]$**	**Calculated K_{sat} $[cm\ s^{-1}]$**	**Saturated volumetric water content θ_s**	**α $[cm^{-1}]$**	**n**
Sand	0.0013	0.0014	0.418	0.153	1.71
Clay	0.0004	0.0010	0.423	0.148	1.66

The hydraulic conductivity decreases as the matric potential decreases from 0 kPa to -75kPa (P<0.001) and is slightly larger in the sand soil compared to the clay soil. The van Genuchten model fits the imaged data well with a slight discrepancy in the WRC at 0 kPa (RMSE=0.016 for the clay soil and RMSE=0.022 for the clay soil). The experimentally measured hydraulic conductivity agreed well with the calculated value for the sand soil. However, the data compares less favourably in the case of the clay soil where the experimentally measured hydraulic conductivity is less than half that of the calculated value.

The differences observed for the clay soil between the experimentally measured hydraulic conductivity and the calculated values are attributed to a combination of image resolution and segmentation limitations. Typically clay soils have much smaller pores than sand soils, due to the differences in particle size and as such will have a large number of pores which are comparable with or below the imaging resolution used in this study. Further complications include partial volume effects, which can cause errors in voxel classification, if the boundary is between two phases with wide ranging attenuation values, such as air and rock [*Ketcham and Carlson*, 2001]. This therefore could lead to an incorrect classification of voxels resulting in either an overestimate or an underestimate of the pore space and pore size distribution due to the effect it has on objects of differing sizes, which may explain why we have an overestimation at the wet end, and underestimation at the dry end. As the calculated hydraulic conductivity is large with respect to the measured value we expect that the pore space is being over estimated in this case.

Deleted: , this

Deleted: and

4.2 Pore characteristics

In order to obtain a better understanding of the pore scale processes which contribute to the macroscopic hydraulic properties we consider the distribution of air and water within the soil matrix on the pore scale. In order to quantify the air and water content we define Air Filled Pores (AFPs) and Water Filled Pores (WFPs) as single connected regions of air or water respectively. We also define the pore space as the union of all the AFPs and WFPs. Throughout this paper when discussing connected regions of water and air we exclusively use this terminology in keeping with the soil science literature. In addition we refer to individual pores within the soil to define simply connected pathways between two distinct points within the pore space. Typically, the pore space contains a single large WFP which contains over 50% of the water within the pore space and a large number of much smaller AFPs and WFPs. The connected WFPs are the main contributor to both the WRC and the hydraulic conductivity calculations. However, insight may be gained into the wetting and drying behaviour of the soils by considering the properties of the AFPs. It is possible to determine the interfacial area between water and air phases [*Costanza-Robinson et al.*, 2008]. However, as previous studies have made the calculations based on porous media other than soil, this is not comparable to the work undertaken in this study. In addition the majority of the previous work in soil [*Falconer et al.*, 2012; *García-Marco et al.*, 2014; *Tucker*, 2014], refer directly to WFPs and AFPs as such it is more meaningful in the context of the literature to consider the WFP and AFP surface area.

Formatted: Font color: Text 1

Formatted: Font color: Text 1

Deleted: researchers working in soil science

Formatted: Font color: Text 1

At 0 kPa we have a residual AFP volume of approximately 6% of the total pore space, see supplementary Figure 3. This volume corresponds to trapped air pockets which, due to the high tortuosity of the soil structure, remain in the pore space at saturation. As the matric potential is made more negative, the total WFP volume decreases and the corresponding AFP volume increases (Figure 6; $P<0.001$). In addition to the change in WFP and AFP volume, the total soil volume is seen to increase by up to 10%. Whilst this may, in part, be attributed to segmentation issues and partial volume effects, it is also likely that changes in soil structure are responsible for this apparent increase. The total AFP volume and the corresponding AFP surface area did not vary significantly across the different soil types (sand and clay). However, the average volume and the corresponding surface area of an individual AFP averaged across all matric potentials shows significant variation across soil types ($P<0.001$) with average AFP volume of 0.00115 mm^3 in the clay soil compared with 0.00163 mm^3 in the sand soil and with average AFP surface area of 0.0109 mm^2 in the clay soil and 0.0182 mm^2 in the sand soil. This greater surface area corresponds to a much greater number of AFPs at -75 kPa in the clay soil (104 pores/mm^3) than the sand soil (55 pores/ mm^3), (P<0.05). The average pore thickness decreased significantly with decreasing matric potential (Figure 7; P<0.001), from an average of 0.030 mm at 0 kPa to 0.026 mm at -75 kPa. There was no significant difference between soil types. At 0 kPa the average pore thickness for the clay soil was 0.027 mm compared to 0.033 mm for sand. At -75 kPa the average pore thickness for the clay and the sand soils was just 0.026 mm.

To highlight the differences in the soil types we classify the AFPs as air filled macro (> 100 μm), air filled meso (30 - 100 μm) and air filled micropores (21 – 30 μm), see supplementary Figure 4. This classification is based on the pore diameter, *i.e.* the maximum sphere diameter which can fit inside the pore. The air filled micropore range is limited by the achievable resolution based on our estimation of image noise (> 2 voxels). As the matric potential is decreased, the total number of AFPs classified into each category changes with an overall increase in the number of air filled macropores seen in the case of the sand soil. In the sand soil there is a linear increase in the percentage of air filled macropores with soil drainage, this was expected due to the high number of macropores throughout the sand structure, which is typically more homogenous compared to the clay. The clay soil had a less regular drainage pattern than the sand soil. There is a linear increase in the air filled micropore percentage as the clay dried. However, the percentage of air filled macropores is quite irregular and can be attributed to the occurrence of crack formation which is more likely in clay soil. The average pore circularity of the AFPs, equation (2), also increased as matric potential decreased. At -75 kPa the AFP space was comprised of pores with an average circularity of 0.78 compared to a circularity value of 0.72 at 0 kPa (P<0.001). Our results also show that at drier matric potentials the shape of the air and water filled pores become increasingly rounded possibly linked to air bubble-style pore formation. This measurement enables us to quantify the influence of pore

Deleted: per

Deleted: per

Deleted: It is possible to determine the interfacial area between water and air phases [*Costanza-Robinson et al.*, 2008], however as previous studies have made the calculations based on glass beads and pure sand mixtures, this is not comparable to the work undertaken in this study. However, further investigation into this measurement for porous media with two fluid flows would be of interest. Our work agrees with Kibbey [2013], in that microscopic surface roughness is likely to have a relatively small effect on the accuracy of the fluid flow at the air and water boundaries providing that the surface scale of the surface roughness is sufficiently small [*Daly and Roose*, 2014]. This means our imaging resolution should not be a limiting consideration on the surfaces obtained [*Brusseau et al.*, 2010]. ¶

Deleted: determined

Deleted: ,

Deleted: t

Deleted: gives

Deleted: a

Deleted: ication

Deleted: of

Deleted: drainage on

shape on soil drainage. However we note this is only a single measure and further descriptors that account for the shape of the soil porous architecture in 3D are required to advance understanding in this area. The 3D connectivity of the WFPs decreased with decreasing matric potential ($P<0.05$), pore connectivity was significantly greater in the clay soil at all matric potentials ($P<0.01$). The differences in the AFP structure in the two soil types are indicative of the soil structure. The clay soil contains a large number of micro-pores which corresponds to the large number of air filled micropores trapped within the soil structure. In contrast the sand soil contains a larger number of meso- and macro-pores causing the air to be contained in relatively few, larger volumes. It is highly likely that the clay soil contained many pores that were too small to be imaged at the achievable resolution in this study.

5. Conclusions

In this paper we have used a combination of CT imaging and mathematical modelling to derive the WRC and unsaturated hydraulic conductivity in contrasting soil textures (*i.e.* clay and sand) and structures (i.*e.* sieved and field structured soil). The ability to non-destructively scan the soil cores and segment the water and air filled pores from the soil matrix combined with the mathematical modelling have provided a unique insight into the WRC and hydraulic properties of contrasting soils. A comprehensive study of the hydraulic properties of different soil types based on a quantitative visual assessment of the soil structure has been carried out across a range of different saturation values. The results predict the increase in hydraulic conductivity with saturation and highlight the structural basis for the differences between sand and clay soils.

Deleted: ,
Deleted: h
Deleted: are urgently required for this type of work
Deleted: .
Deleted: more
Deleted: the

The data obtained via CT imaging allows us to visualise the soil structure in 3D and, hence, to measure the effects of pore geometry on the WRC. Using the scanned geometry combined with detailed mathematical modelling, the unsaturated hydraulic conductivity and, hence, hydraulic conductivities were obtained at the precise measured matric potentials. These values are not easily measured in the laboratory through experimentation alone. Using the measured saturated hydraulic conductivity and typical soil parameters we have compared the computed values against the van Genuchten model. The simulated values compared well with the measured saturated hydraulic conductivity values. The calculated hydraulic properties of the clay soil against the van Genuchten model compare well. However, in the case of the sand soil, the calculated values are lower than those obtained using the van Genuchten model. This highlights the potential structural differences between two soils of a particular textural class and the potential role played by the micro-porous structure of the aggregates which are currently below the imaging resolution of CT for this sample size.

Deleted: structural

The combination of CT imaging and modelling provides a new level of understanding of the role that structure plays in the averaged properties of soil. The WRC has been obtained via CT imaging and provides a detailed geometric representation of how the water is retained in pores of different sizes. A downside to the imaging approach is the time investment required to collect the data. However, this is comparable to the conventional laboratory method as the majority of time is spent allowing the sample to equilibrate. However, this detailed information on the pore-scale architecture represents a significant development in our ability to study soil systems which will continue to advance pore scale modelling by providing three dimensional geometries against which the numerical models can be tested [19].

Deleted: used in this paper

Deleted: the

Deleted: d pore

Deleted: The

6. Acknowledgements

The authors acknowledge the use of the IRIDIS High Performance Computing Facility, and associated support services at the University of Southampton, in the completion of this work. This project was funded by BBSRC BB/J000868/1, a collaborative project between Southampton and Nottingham, PI and overall lead Roose. All reconstructed scan data will be available on request by emailing microct@nottingham.ac.uk. The authors extend their thanks to the anonymous reviewers for constructive feedback on their manuscript.

Table A1. Values of parameters used in numerical calculations

Constant	Value	Units	Description
ρ^w	10^3	kg m^{-3}	Density of water
ρ^a	1.2	kg m^{-3}	Density of air
μ^w	10^{-3}	kg m^{-1} s^{-}	Viscosity of water
μ^a	20×10^{-6}	kg m^{-1} s^{-}	Viscosity of air
$\tilde{g}$	9.8	m s^{-2}	Acceleration due to gravity
r_y	100×10^{-6}	m	Typical pore radius
L_y	10^{-3}	m	Typical size of microscale geometry
L_x	10^{-1}	m	Typical size of macroscale geometry
$\tilde{\gamma}$	7.28×10^{-2}	kg s^{-2}	Surface tension
$\tilde{\kappa}$	10^4	m^{-1}	Curvature
ϵ	10^{-2}		Ratio of geometry sizes
κ	2.97×10^2		Scaled surface tension-curvature product
$\lvert\boldsymbol{g}\rvert$	1		Scaled gravitational force
δ_u	0.16		Typical velocity ratio
δ_p	8.33		Typical pressure ratio

Appendix

The starting point is the non-dimensional Stokes equations using the scaling given in [*Daly and Roose*, 2014]. The dimensional variables, denoted with a $\tilde{\cdot}$, are scaled using

$$\boldsymbol{v}^w = \frac{4\mu^w}{\rho^w \tilde{g} r_y^2}\,\tilde{\boldsymbol{v}}^w, \qquad p^w = \left(\frac{L_x}{L_y}\right)\frac{4L_y}{\rho^w \tilde{g} r_y^2}\,\tilde{p}^w,$$

$$\boldsymbol{v}^a = \left(\frac{L_x}{L_y}\right)\frac{4\mu^a}{\rho^a \tilde{g} r_y^2}\,\tilde{\boldsymbol{v}}^a, \qquad p^a = \left(\frac{L_x}{L_y}\right)^2\frac{4L_y}{\rho^a \tilde{g} r_y^2}\,\tilde{p}^a,$$

$$t = \left(\frac{L_x}{L_y}\right)\frac{\rho^w r_y^2\,\tilde{g}}{4\mu^w L_y}\,\tilde{t},$$

where $\boldsymbol{v}^w$ and $\boldsymbol{v}^a$ are the water and air velocities, p^w and p^a are the water and air pressures, t is the dimensionless time and the remaining parameters are listed in table A1 and the non-dimensional constants are

$$\kappa = \left(\frac{L_y}{L_x}\right)\frac{4L_y\,\tilde{\gamma}}{\rho^w r_y^2\,\tilde{g}}\tilde{\kappa}, \qquad \boldsymbol{g} = \frac{\hat{\boldsymbol{e}}_x L_y^3}{r_y^2 L_x}, \qquad \delta_u = \left(\frac{L_y}{L_x}\right)\frac{\rho^w\mu^a}{\rho^a\mu^w}, \qquad \delta_p = \left(\frac{L_y}{L_x}\right)\frac{\rho^w}{\rho^a},$$

Typical values for the non-dimensional numbers are given in table A1. The resulting non-dimensional Stokes equations are:

$$\epsilon\boldsymbol{\nabla}\cdot\sigma^w - \boldsymbol{\nabla}p^w = \epsilon\boldsymbol{g} \qquad \boldsymbol{x}\in\Omega_w, \qquad \text{(A1a)}$$

$$\epsilon\boldsymbol{\nabla}\cdot\sigma^a - \boldsymbol{\nabla}p^a = \epsilon^2\boldsymbol{g} \qquad \boldsymbol{x}\in\Omega_a, \qquad \text{(A1b)}$$

$$\epsilon\phi\frac{\partial S^w}{\partial t} + \boldsymbol{\nabla}\cdot\boldsymbol{v}^w = 0, \qquad \boldsymbol{x}\in\Omega_w, \qquad \text{(A1c)}$$

$$\epsilon\phi\frac{\partial s^a}{\partial t}+\delta_u\boldsymbol{\nabla}\cdot\boldsymbol{v}^a=0, \qquad \boldsymbol{x}\in\Omega_a, \qquad \text{(A1d)}$$

$$\boldsymbol{v}^w=0, \qquad \boldsymbol{v}^a=0, \qquad \boldsymbol{x}\in\Gamma_s, \qquad \text{(A1e)}$$

$$\hat{\boldsymbol{n}}\cdot\boldsymbol{v}^w=0, \qquad \hat{\boldsymbol{n}}\cdot\boldsymbol{v}^a=0, \qquad \boldsymbol{x}\in\Gamma_{aw}, \qquad \text{(A1f)}$$

$$\hat{\boldsymbol{\tau}}\cdot[\boldsymbol{v}^w-\delta_u\boldsymbol{v}^a]=0, \qquad \boldsymbol{x}\in\Gamma_{aw}, \qquad \text{(A1g)}$$

$$\hat{\boldsymbol{n}}\cdot\left[(\epsilon\sigma^w-Ip^w)-\delta_p(\epsilon\sigma^a-Ip^a)\right]=\hat{\boldsymbol{n}}\kappa, \qquad \boldsymbol{x}\in\Gamma_{aw}, \qquad \text{(A1h)}$$

combined with periodic boundary conditions in the x y and z directions. To simplify the problem we notice that $\delta_u^{-1}<1$ and $\delta_p<1$ and, therefore, they can be neglected to first approximation. The result is that the air and water velocities decouple we need only consider the flow of water through the soil. The air velocity could in principle be calculated as a perturbation of order δ_u which in turn would create a water velocity perturbation of order δ_u/δ_p. However, we expect that this perturbation will be small with respect to the uncertainty in the segmentation and the temperature dependent variations of the water viscosity. The simplified equations are:

$$\epsilon\nabla^2\boldsymbol{v}^w-\boldsymbol{\nabla}p^w=\epsilon\boldsymbol{g} \qquad x\in\Omega_w, \qquad \text{(A2a)}$$

$$\boldsymbol{\nabla}\cdot\boldsymbol{v}^w=0, \qquad x\in\Omega_w, \qquad \text{(A2e)}$$

$$\boldsymbol{v}^w=0, \qquad x\in\Gamma_s, \qquad \text{(A2f)}$$

$$\boldsymbol{v}^w=0, \qquad x\in\Gamma_{aw}, \qquad \text{(A2g)}$$

We expand the gradient operator $\boldsymbol{\nabla}=\epsilon\boldsymbol{\nabla}_x+\boldsymbol{\nabla}_y$ and look for a power series solution to equations (A4) of the form

$$\boldsymbol{v}^w=\boldsymbol{v}_0^w+\epsilon\boldsymbol{v}_1^w+O(\epsilon^2) \qquad \text{(A3a)}$$
$$p^w=p_0^w+\epsilon p_1^w+O(\epsilon^2) \qquad \text{(A3b)}$$

Substituting equations (A3) into equations (A2) and retaining terms $O(\epsilon^0)$ we obtain $\boldsymbol{\nabla}_y p_0^w=0$, *i.e.*, the largest component of the pressure is constant over the microscale. Expanding to $O(\epsilon^1)$ we effectively convert the leading order pressure drop into a body force and obtain

$$\boldsymbol{v}_0^w=\sum_{k=1}^{3}\boldsymbol{v}_k\partial_{x_k}p_0^w$$

Where $\boldsymbol{v}_k$ satisfy the cell problem

$$\nabla_y^2\boldsymbol{v}_k-\boldsymbol{\nabla}_y\pi_k^w=\hat{\boldsymbol{e}}_k, \qquad \boldsymbol{x}\in\Omega_w, \qquad \text{(A4a)}$$

$$\boldsymbol{\nabla}_y\cdot\boldsymbol{v}_k=0, \qquad \boldsymbol{x}\in\Omega_w, \qquad \text{(A4b)}$$

$$\boldsymbol{v}_k=0, \qquad \boldsymbol{x}\in\Gamma_s, \qquad \text{(A4c)}$$

$$\boldsymbol{v}_k = 0, \qquad \boldsymbol{x} \in \Gamma_{aw}, \qquad \text{(A4d)}$$

$$\boldsymbol{v}_k, \pi_k^w \text{ periodic with period 1} \qquad \text{(A4e)}$$

Averaging the velocity over the unit cell we obtain the non-dimensional form of Darcy's law for the average velocity

$$\boldsymbol{u}_0^w = \int_\Omega \boldsymbol{v}_k \otimes \hat{\boldsymbol{e}}_k \, dy \, (\boldsymbol{\nabla}_x p_0^w + \boldsymbol{g})$$

which in dimensional form is equation (3) and (4) in the main paper.

As discussed in the main text we impose periodicity via reflection of the geometry about the x, y and z axis. The result is that the velocity is, for the k-th cell problem, the pressure correction π_k^w is even odd in the direction x_k and even in the direction x_j for $j \neq k$. Similarly we find that the k-th component of the velocity, $\hat{\boldsymbol{e}}_k \cdot \boldsymbol{v}_k$ is even in all directions. The remaining velocity components, $\hat{\boldsymbol{e}}_j \cdot \boldsymbol{v}_k$ for $j \neq k$, are odd in the directions x_k and x_j, however, they are even in the direction x_p for $p \neq k$ and $p \neq j$. Specifically the resulting boundary equations and boundary conditions are:

$$\nabla_y^2 \boldsymbol{v}_k - \boldsymbol{\nabla}_y \pi_k^w = \hat{\boldsymbol{e}}_k, \qquad \boldsymbol{x} \in \Omega_w, \qquad \text{(A5a)}$$

$$\boldsymbol{\nabla}_y \cdot \boldsymbol{v}_k = 0, \qquad \boldsymbol{x} \in \Omega_w, \qquad \text{(A5b)}$$

$$\boldsymbol{v}_k = 0, \qquad \boldsymbol{x} \in \Gamma_s, \qquad \text{(A5c)}$$

$$\boldsymbol{v}_k = 0, \qquad \boldsymbol{x} \in \Gamma_{aw}, \qquad \text{(A5d)}$$

$$\pi_k^w = 0, \; \frac{\partial}{\partial x_k}(\hat{\boldsymbol{e}}_k \cdot \boldsymbol{v}_k) = 0, \; \hat{\boldsymbol{e}}_j \cdot \boldsymbol{v}_k = 0, j \neq k \qquad \boldsymbol{x} \in \partial x_k \qquad \text{(A5e)}$$

$$\frac{\partial}{\partial x_j}\pi_k^w = 0, \; \frac{\partial}{\partial x_p}\left(\hat{\boldsymbol{e}}_p \cdot \boldsymbol{v}_k\right) = 0, \hat{\boldsymbol{e}}_j \cdot \boldsymbol{v}_k = 0, p \neq k, , p \neq j \qquad \boldsymbol{x} \in \partial x_j \qquad \text{(A5f)}$$

where ∂x_k is the boundary located at $x_k = 0$ and $x_k = 1/2$, ∂x_j is the union of the boundaries located at $x_j = 0$ and $x_j = 1/2$ for $j \neq k$.

7. References

Aravena, J., M. Berli, S. Ruiz, F. Suarez, T. Ghezzehei, and S. Tyler (2014), Quantifying coupled deformation and water flow in the rhizosphere using X-ray microtomography and numerical simulations, *Plant and Soil*, *376*(1-2), 95-110.
Aravena, J. E., M. Berli, T. A. Ghezzehei, and S. W. Tyler (2011), Effects of Root-Induced Compaction on Rhizosphere Hydraulic Properties - X-ray Microtomography Imaging and Numerical Simulations, *Environmental Science & Technology*, *45*(2), 425-431.
Arbogast, T., and H. L. Lehr (2006), Homogenization of a Darcy–Stokes system modeling vuggy porous media, *Computational Geosciences*, *10*(3), 291-302.
Blunt, M. J. (2001), Flow in porous media—pore-network models and multiphase flow, *Current opinion in colloid & interface science*, *6*(3), 197-207.
Blunt, M. J., B. Bijeljic, H. Dong, O. Gharbi, S. Iglauer, P. Mostaghimi, A. Paluszny, and C. Pentland (2013), Pore-scale imaging and modelling, *Advances in Water Resources*, *51*, 197-216.
Bryant, S., and M. Blunt (1992), Prediction of relative permeability in simple porous media, *Physical Review A*, *46*(4), 2004.
Bryant, S., D. Mellor, and C. Cade (1993a), Physically representative network models of transport in porous media, *AIChE Journal*, *39*(3), 387-396.
Bryant, S., P. King, and D. Mellor (1993b), Network model evaluation of permeability and spatial correlation in a real random sphere packing, *Transport in Porous Media*, *11*(1), 53-70.
Clausnitzer, V., and J. W. Hopmans (2000), Pore-scale measurements of solute breakthrough using microfocus X-ray computed tomography, *Water Resources Research*, *36*(8), 2067-2079.
Costanza-Robinson, M. S., K. H. Harrold, and R. M. Lieb-Lappen (2008), X-ray microtomography determination of air− water interfacial area− water saturation relationships in sandy porous media, *Environmental science & technology*, *42*(8), 2949-2956.
Crestana, S., S. Mascarenhas, and R. S. Pozzi-Mucelli (1985), Static and dynamic 3 dimensional studies of water in soil using computed tomographic scanning, *Soil Science*, *140*, 326-332.
Daly, K. R., and T. Roose (2014), Multiscale modelling of hydraulic conductivity in vuggy porous media, *Proceedings of the Royal Society A: Mathematical, Physical and Engineering Science*, *470*(2162).
Doube, M., M. M. Kłosowski, I. Arganda-Carreras, F. P. Cordelières, R. P. Dougherty, J. S. Jackson, B. Schmid, J. R. Hutchinson, and S. J. Shefelbine (2010), BoneJ: Free and extensible bone image analysis in ImageJ, *Bone*, *47*(6), 1076-1079.
Falconer, R. E., A. N. Houston, W. Otten, and P. C. Baveye (2012), Emergent Behavior of Soil Fungal Dynamics: Influence of Soil Architecture and Water Distribution, *Soil Science*, *177*(2), 111-119 110.1097/SS.1090b1013e318241133a.
Fatt, I. (1956), The network model of porous media.
Ferreira, T. A. W. R., and W. Rasband (2011), The ImageJ User Guide, Version 1.45., (http://rsbweb.nih.gov/ij/docs/user-guide.pdf).
Fowler, A. C. (1997), *Mathematical models in the applied sciences*, Cambridge University Press, U.K.
Gao, W., T. Ren, A. G. Bengough, L. Auneau, C. W. Watts, and W. R. Whalley (2012), Predicting Penetrometer Resistance from the Compression Characteristic of Soil, *Soil Science Society of America Journal*, *76*(2), 361-369.
García-Marco, S., S. R. Ravella, D. Chadwick, A. Vallejo, A. S. Gregory, and L. M. Cárdenas (2014), Ranking factors affecting emissions of GHG from incubated agricultural soils, *European Journal of Soil Science*, *65*(4), 573-583.
Gardner, W. H. (1965), Water Content, in *Methods of Soil Analysis. Part 1. Physical and Mineralogical Properties, Including Statistics of Measurement and Sampling*, edited by C. A. Black, pp. 82-127, American Society of Agronomy, Soil Science Society of America.

Haugen, Å., N. Mani, S. Svenningsen, B. Brattekås, A. Graue, G. Ersland, and M. Fernø (2014), Miscible and Immiscible Foam Injection for Mobility Control and EOR in Fractured Oil-Wet Carbonate Rocks, *Transport in Porous Media*, *104*(1), 109-131.

Helliwell, J. R., A. J. Miller, W. R. Whalley, S. J. Mooney, and C. J. Sturrock (2014), Quantifying the impact of microbes on soil structural development and behaviour in wet soils, *Soil Biology and Biochemistry*, *74*(0), 138-147.

Hornung, U. (1997), *Homogenization and porous media*, Springer, Berlin, Germany.

Houston, A. N., W. Otten, P. C. Baveye, and S. Hapca (2013), Adaptive-window indicator kriging: A thresholding method for computed tomography images of porous media, *Computers & Geosciences*, *54*(0), 239-248.

Iassonov, P., T. Gebrenegus, and M. Tuller (2009), Segmentation of X-ray computed tomography images of porous materials: A crucial step for characterization and quantitative analysis of pore structures, *Water Resources Research*, *45*(9), W09415.

Keller, J. B. (1980), Darcy's law for flow in porous media and the two-space method, paper presented at Nonlinear partial differential equations in engineering and applied science (Proc. Conf., Univ. Rhode Island, Kingston, RI, 1979), Dekker New York.

Ketcham, R. A., and W. D. Carlson (2001), Acquisition, optimization and interpretation of X-ray computed tomographic imagery: applications to the geosciences, *Computers & Geosciences*, *27*(4), 381-400.

Keyes, S. D., K. R. Daly, N. J. Gostling, D. L. Jones, P. Talboys, B. R. Pinzer, R. Boardman, I. Sinclair, A. Marchant, and T. Roose (2013), High resolution synchrotron imaging of wheat root hairs growing in soil and image based modelling of phosphate uptake, *New Phytologist*, *198*(4), 1023-1029.

Mooney, S. J. (2002), Three-dimensional visualization and quantification of soil macroporosity and water flow patterns using computed tomography, *Soil Use and Management*, *18*(2), 142-151.

Mooney, S. J., and C. Morris (2008), A morphological approach to understanding preferential flow using image analysis with dye tracers and X-ray Computed Tomography, *CATENA*, *73*(2), 204-211.

Mooney, S. J., T. P. Pridmore, J. Helliwell, and M. J. Bennett (2012), Developing X-ray Computed Tomography to non-invasively image 3-D root systems architecture in soil, *Plant and Soil*, *352*(1-2), 1-22.

Panfilov, M. (2000), *Macroscale models of flow through highly heterogeneous porous media*, Springer.

Pavliotis, G., and A. Stuart (2008), *Multiscale Methods: Averaging and Homogenization*, Springer.

Ramstad, T., P. E. Oren, and S. Bakke (2010), Simulation of Two-Phase Flow in Reservoir Rocks Using a Lattice Boltzmann Method, *Spe Journal*, *15*(4), 923-933.

Reinhart, K. G. (1961), The Problem of Stones in Soil-Moisture Measurement1, *Soil Sci. Soc. Am. J.*, *25*(4), 268-270.

Rogasik, H., J. W. Crawford, O. Wendroth, I. M. Young, M. Joschko, and K. Ritz (1999), Discrimination of soil phases by dual energy x-ray tomography, *Soil Science Society of America Journal*, *63*(4), 741-751.

Rowell, D. L. (1994), *Soil science : methods and applications* Longman Scientific & Technical ; Prentice Hall.

Taylor, H. M., M. G. Huck, B. Klepper, and Z. F. Lund (1970), Measurement of Soil-grown Roots in a Rhizotron, *Agron. J.*, *62*(6), 807-809.

Tippkötter, R., T. Eickhorst, H. Taubner, B. Gredner, and G. Rademaker (2009), Detection of soil water in macropores of undisturbed soil using microfocus X-ray tube computerized tomography (μCT), *Soil and Tillage Research*, *105*(1), 12-20.

Tucker, C. (2014), Reduction of air- and liquid water-filled soil pore space with freezing explains high temperature sensitivity of soil respiration below 0 °C, *Soil Biology and Biochemistry*, *78*(0), 90-96.
van Genuchten, M. T. (1980), A Closed-form Equation for Predicting the Hydraulic Conductivity of Unsaturated Soils1, *Soil Sci. Soc. Am. J.*, *44*(5), 892-898.
Wildenschild, D., J. W. Hopmans, M. L. Rivers, and A. J. R. Kent (2005), Quantitative Analysis of Flow Processes in a Sand Using Synchrotron-Based X-ray Microtomography, *Vadose Zone J.*, *4*(1), 112-126.
Wildenschild, D., C. M. P. Vaz, M. L. Rivers, D. Rikard, and B. S. B. Christensen (2002), Using X-ray computed tomography in hydrology: systems, resolutions, and limitations, *Journal of Hydrology*, *267*(3–4), 285-297.
Zappala, S., J. R. Helliwell, S. R. Tracy, S. Mairhofer, C. J. Sturrock, T. Pridmore, M. Bennett, and S. J. Mooney (2013), Effects of X-Ray Dose On Rhizosphere Studies Using X-Ray Computed Tomography, *PLoS ONE*, *8*(6), e67250.

8. Figures

Figure 1. Outline of steps used in the subsampling, meshing and solution of cell problem. Figures (a) and (b) show the subsampling of a 1.2 mm side length cube of the segmented .stl file. Figure (c) shows the mesh generation. Figures (d) and (e) show the generation of a truly periodic geometry through translation (d) and reflection (e), the original volume mesh is shown in a lighter shade. Figure (f) shows the numerical solution for the local velocity magnitude in the subsampled soil.

Figure 2. Water release characteristic of the sand and clay sieved (a) and field structured (b) soils fitted to the van Genuchten (VG) curve. Error bars associated with histograms show one standard deviation. Note the different scaling on the y axis for figures (a) and (b).

Figure 3. Greyscale images showing examples of field structured (a) & (b) and sieved (c) & (d) clay (a) & (c) sand soil (b) & (d) at -75 kPa. Scale bar = 0.25 mm.

Figure 4. Hydraulic conductivity of field structured sand and clay soils averaged over all directions for decreasing j corresponding to increasing volume. The dots show the result from each of the cubic volumes, the lines show the average. The corresponding saturated hydraulic conductivity measured for the sand and clay soils are 1.3×10^{-3} cm s^{-1} and 0.4×10^{-3} cm s^{-1} respectively.

Deleted: s

Figure 5. Hydraulic conductivity of field structured sand and clay soils as a function of matric potential.

Figure 6. 3D core section of a sand (a) and clay (b) soil sample at the specific matric potentials from saturation (left) to drier (right). Segmented phases are coloured brown (soil), blue (water filled pores) and black (air filled pores). Scale bar = 5 mm.

Figure 7. 3D pore thickness heat maps for a representative sand (a-c) and clay (e-f) sample at 0 (a, d), -20 (b, e) and -75 (c, f) kPa. (g) total air filled pore volume (bars) and average individual pore volumes (lines) for sand and clay soil. Error bars associated with histograms show one standard deviation.

Figure 1.

Deleted: ¶

Deleted: ¶
Page Break
¶

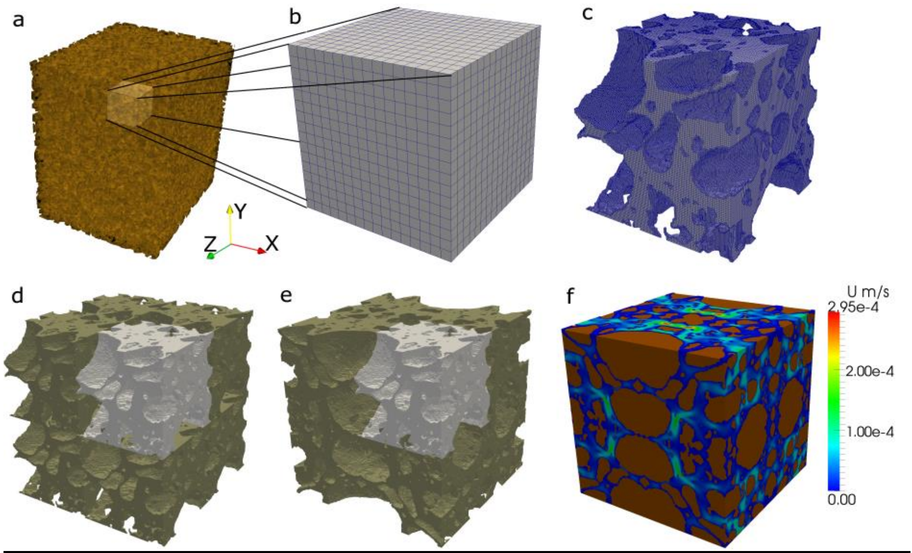
a
b
c
Y
Z
X
d
e
f
U m/s
2.95e-4
2.00e-4
1.00e-4
0.00

Figure 2.

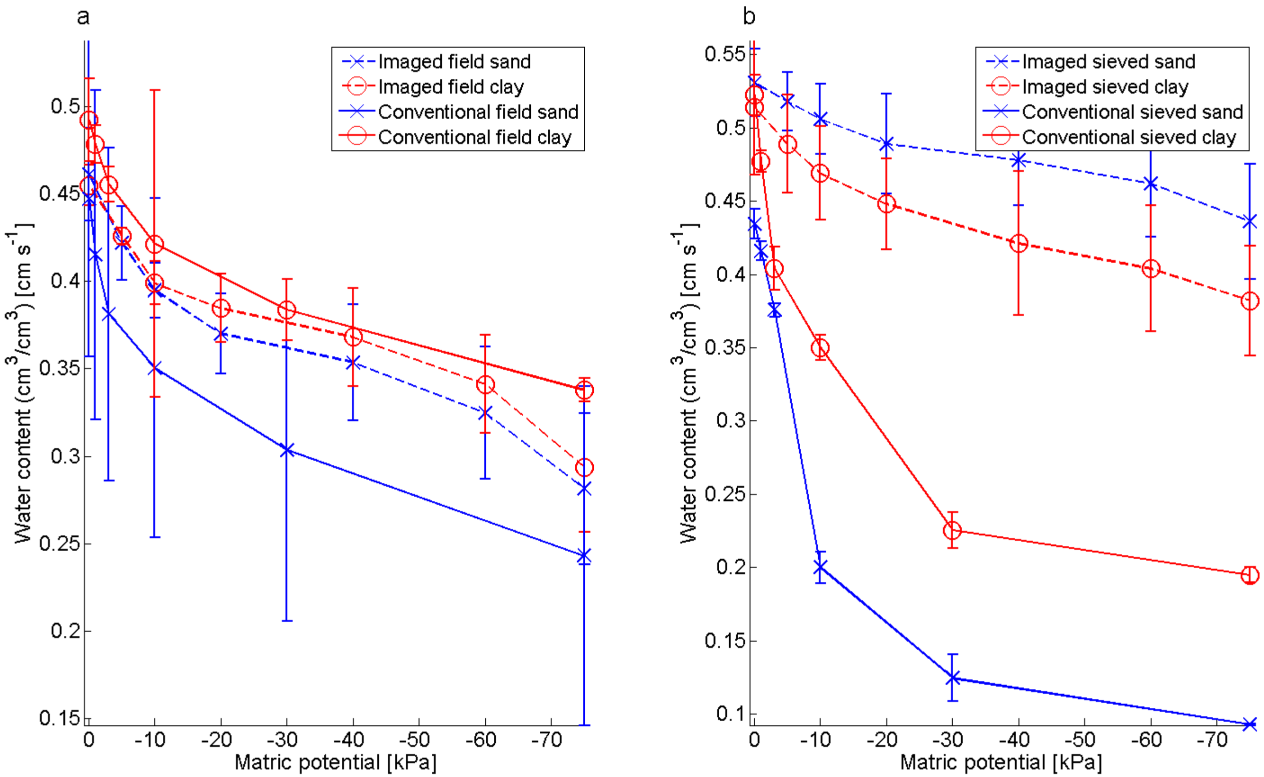

Deleted:

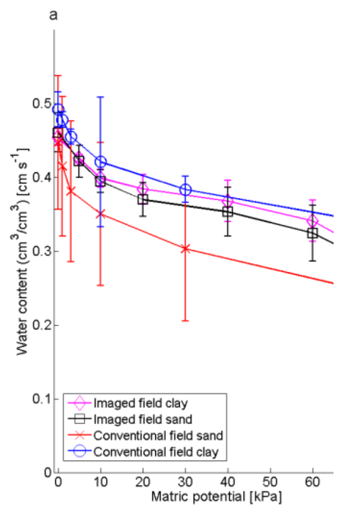

Deleted:

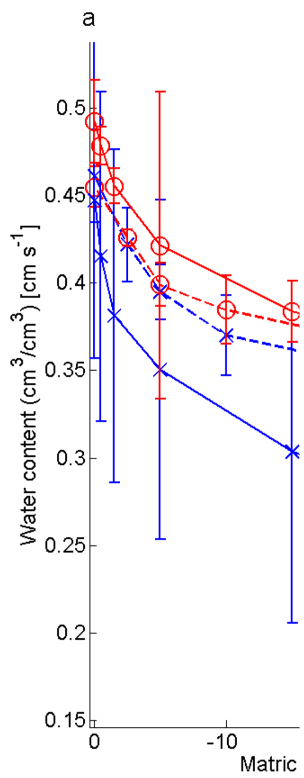

Deleted: ¶

Deleted: ¶

Figure 3.

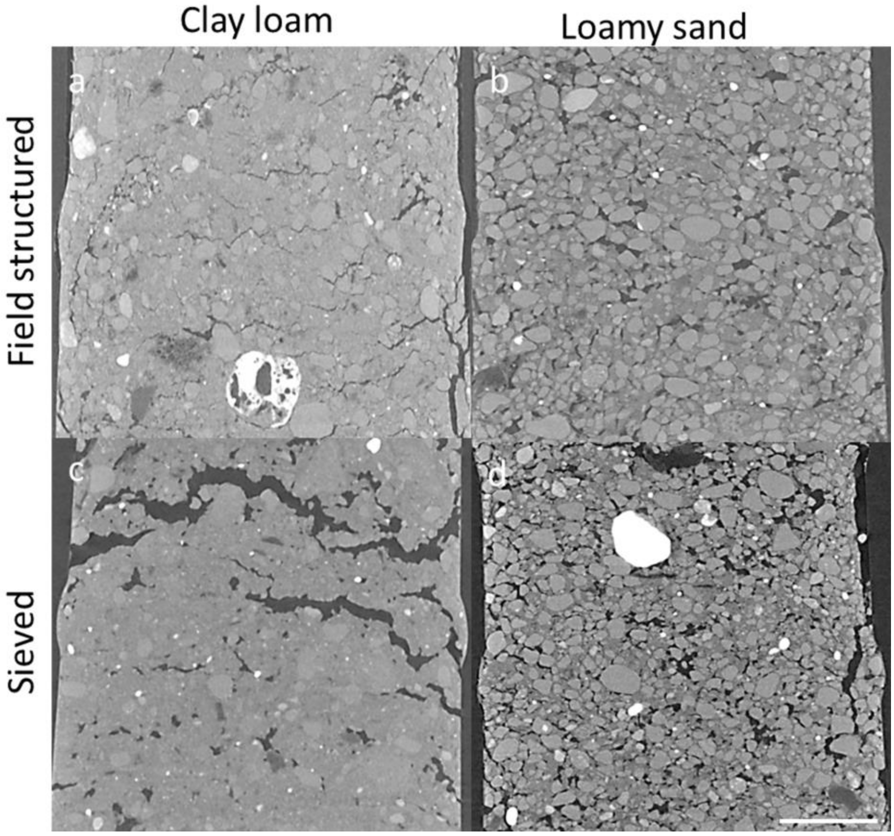

Figure 4.

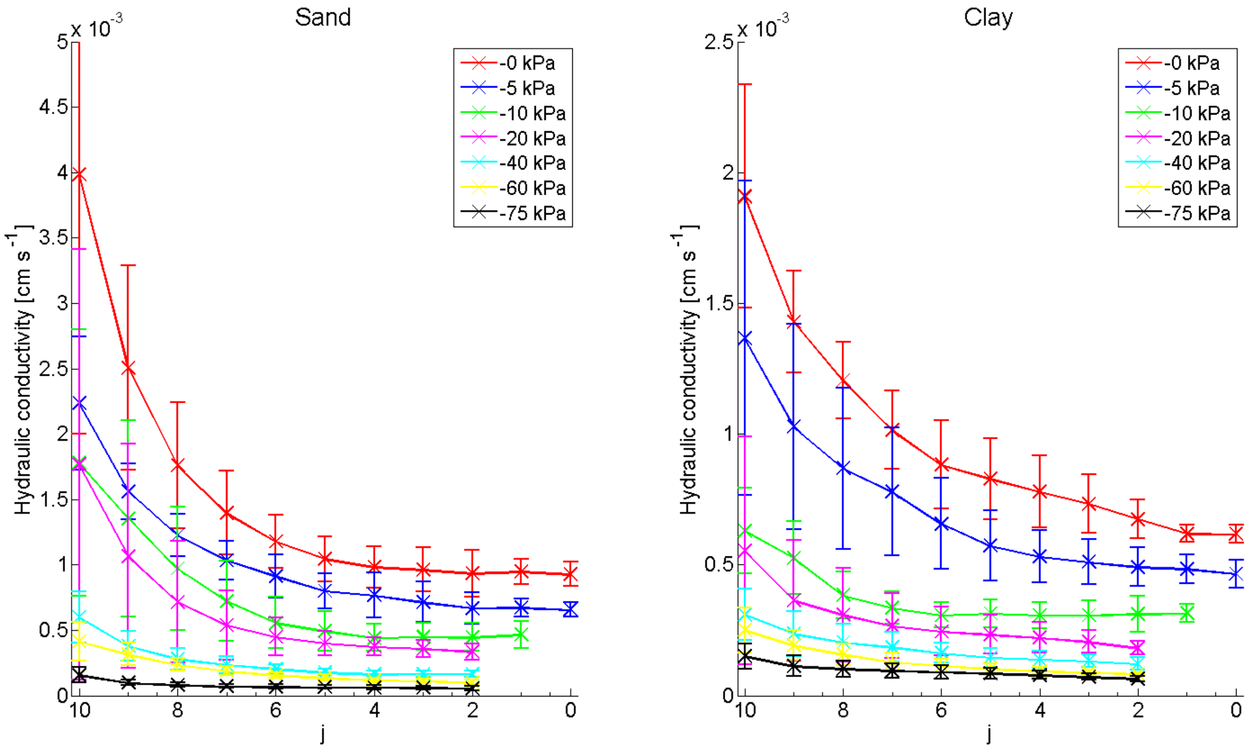

Deleted:

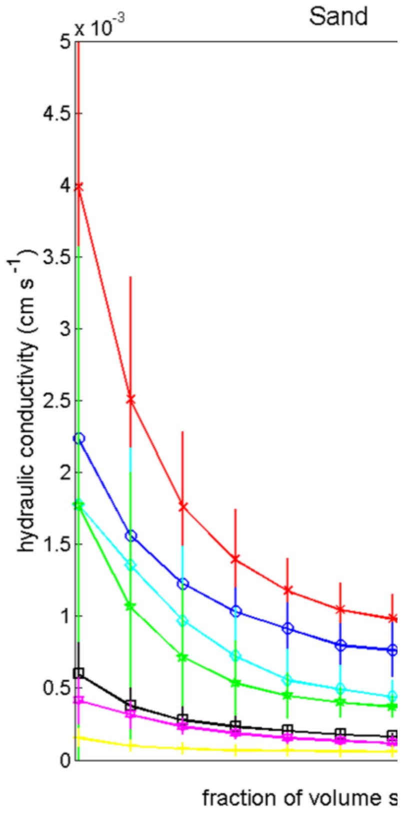

Figure 5.

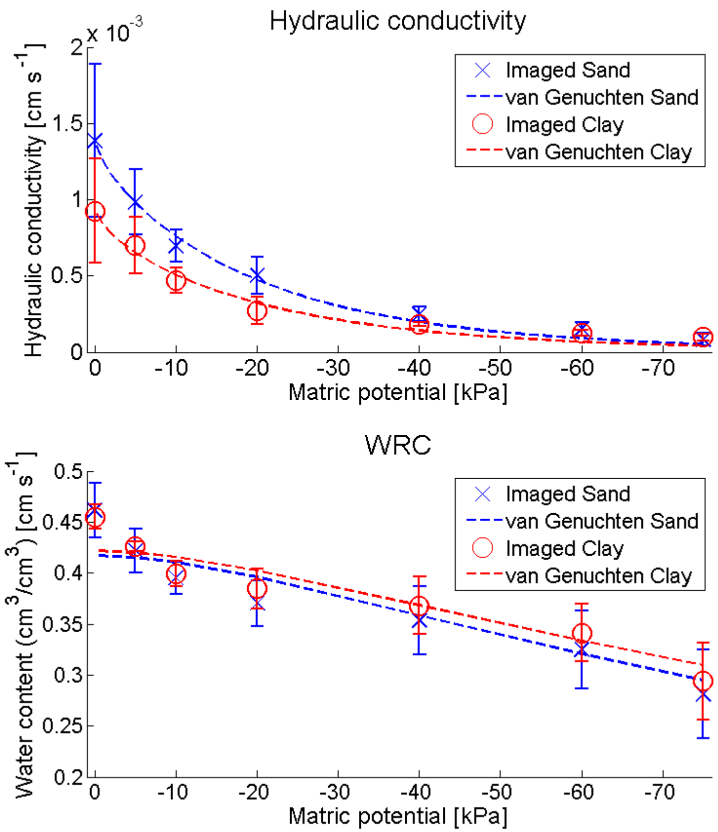

Deleted:

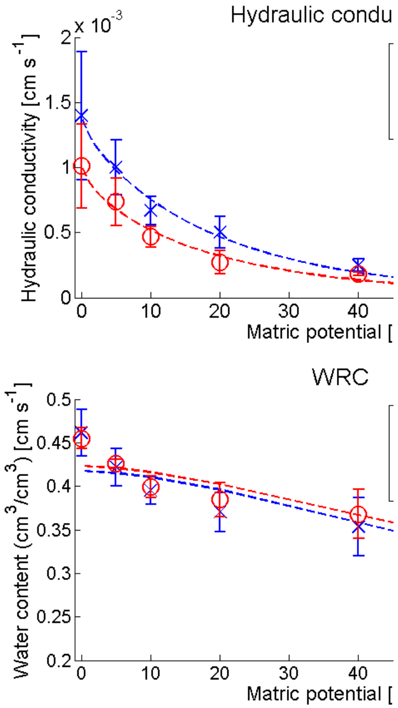

Figure 6.

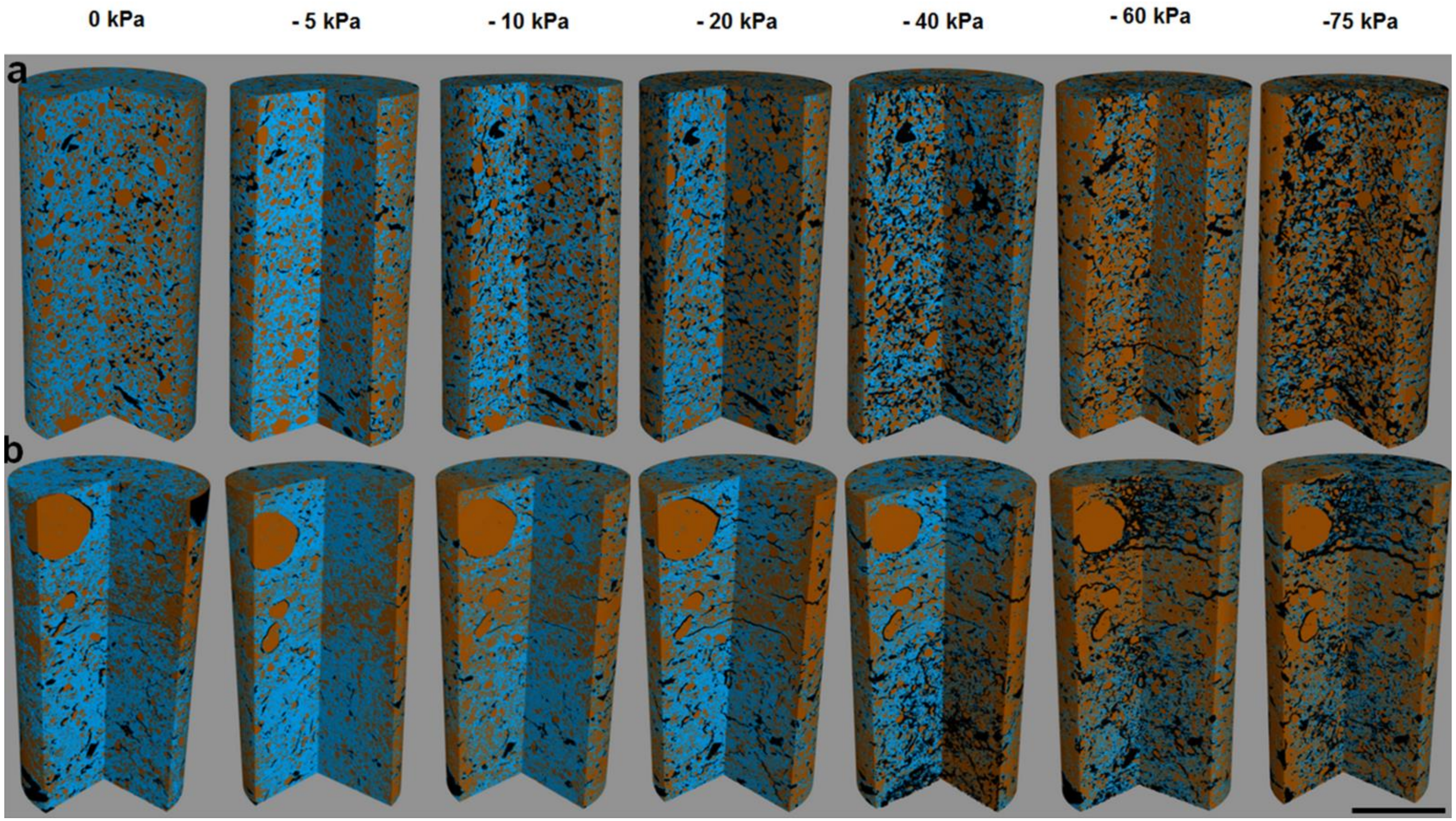

Deleted: ¶
¶

Figure 7.

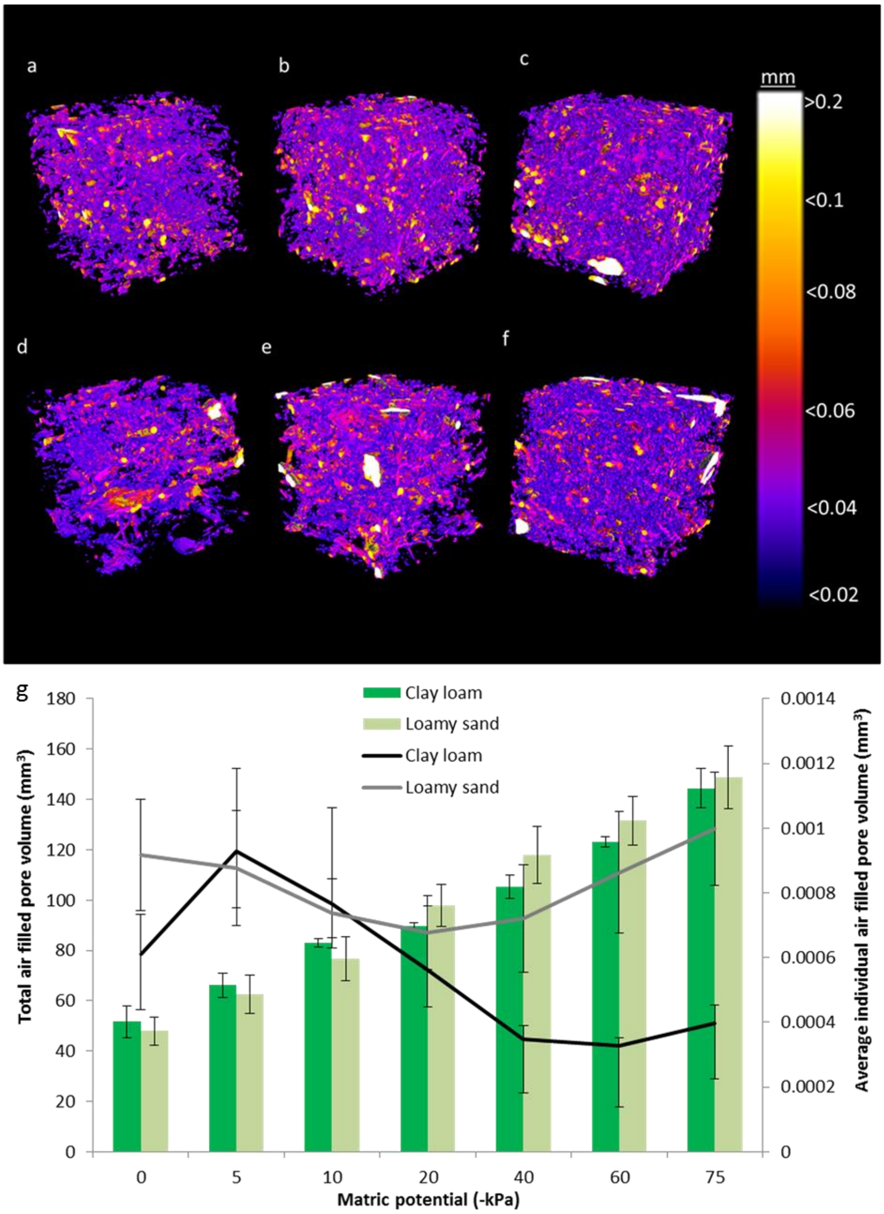

Deleted: Section Break (Next Page)

Formatted: Normal, No bullets or numbering

Formatted: Font: Bold